Selective Capture of Phenol from Biofuel Using Protonated Faujasite Zeolites with Different Si/Al Ratios

Ibrahim Khalil, Hicham Jabraoui, Guillaume Maurin, Sébastien Lebègue, Michael Badawi, Karine Thomas, Françoise Maugé

Selective Capture of Phenol from Biofuel using Protonated Faujasite Zeolites with different Si/Al ratios

Ibrahim Khalil[1], Hicham Jabraoui[2], Guillaume Maurin[3], Sébastien Lebègue[2], Michael Badawi[2*], Karine Thomas[1*], Francoise Maugé[1]

[1]Laboratoire Catalyse et Spectrochimie, ENSICAEN, Université de Caen Normandie, CNRS, 6, bd du Maréchal Juin, 14050 Caen, France

[2] Laboratoire Physique et Chimie Théoriques (LPCT) UMR 7019 CNRS, Université de Lorraine, F-54000 Nancy, France

[3] Institut Charles Gerhardt Montpellier UMR 5253 CNRS UM ENSCM, Université Montpellier, Place E. Bataillon, 34095, Montpellier Cedex 05, France.

*Corresponding authors: karine.thomas@ensicaen.fr ; michael.badawi@univ-lorraine.fr

Abstract

The purification of biofuels becomes a challenging issue because of the harmfulness of remaining phenolic molecules for human health and engines. To this end, protonic Y zeolites with different Si/Al ratios were explored as effective adsorbent materials to remove phenol from isooctane solution by using a dual experimental/computational strategy. Phenol was selectively removed from isooctane over HY and USY zeolites with a maximal adsorption capacity of 2.2 mmol.g^{-1}, that corresponds to 3-4 phenol molecules per zeolitic supercage. The adsorption equilibrium was reached faster over dealuminated zeolites, due to the presence of large pores at the expense of microporosity as well as a low density of acidic sites. We further evidence that the presence of acid sites limits the regeneration capacity since phenol strongly adsorbed on both Brønsted and Lewis acid sites. USY zeolite with the highest Si/Al ratio presents the best regeneration capacity since it has the lower aluminum loading. A fundamental understanding of these performances was obtained by coupling characterization (Infrared Spectroscopy, breakthrough curves and desorption experiments) and modeling tools (Grand Canonical Monte Carlo and Density Functional Theory).

KEYWORDS: Bio-fuel, phenol, adsorption, breakthrough curves, HY zeolites, USY zeolites, acidity, IR, simulations, DFT, Monte Carlo.

1. Introduction

Worldwide energy demand is expected to rise by roughly 55% from 2010 to 2040,[1] inducing a growth in the fossil fuel consumption known as the first responsible of the greenhouse gas emissions.[2] In such a context, there is a strong incentive to develop processes for environmentally friendly renewable fuel sources.[3–5] Hence, the use of liquid biofuels is a way to contribute to the reduction of greenhouse gas emissions.[6,7] Currently, a significant effort is deployed on processing second generation biofuel production i.e that is issued from non-edible biomass as lignocellulosic biomass, wood, agricultural waste, etc.[1,8] Oils obtained from biomass pyrolysis present physicochemical and rheological properties similar to crude oils.[9] However, their high oxygen contents (20-55 wt.%),[4,10] limit their uses (instability, corrosiveness and low energetic power).[11] To remove oxygen and to obtain bio-oils with characteristics compatible with fuels issued from crude oil feedstock, pyrolytic bio-oils can be mixed to vacuum gas oil (VGO) with different VGO/HDO ratios for being co-processed in a FCC unit. [1,2,12,9,13] Thanks to the hydrogen transfer that occurs during the FCC process, a large fraction of oxygen is removed leading to an oxygen amount of the refined biofuels ranging from 0.5 wt.% to 7 wt.%.[12] The residual oxygen-containing compounds are mainly substituted-phenol type molecules.[2,12] It has been recently shown that, even in small concentration, these oxygenated impurities decrease the motor efficiency and produce toxic exhaust gas after bio-fuel combustion.[1] This critically urges for the elimination of phenol-type compounds to obtain ultra-pure bio-fuel. In this work, we propose to tackle this important issue by envisaging a physisorption-based separation process involving the use of a porous material as adsorbent.

Conversely to catalytic reactions, adsorption is a low-energy consuming process. Moreover, selective adsorption allows concentrating the undesired product that can be further valorized for other applications. The adsorbent must present high adsorption capacity as well as high selectivity.[14] In addition, regeneration under mild conditions is an important property of the adsorbent that will allow

the adsorption process to be repeated on several cycles.[15–17] Most of the works on the selective capture of phenol have been reported on aqueous solutions and in particular from wastewater.[15,16,18]

Khalid et al.[16] studied the effect of Si/Al ratio of Y zeolites on the selective adsorption of phenol from wastewater. They show that over the zeolites with high aluminum loading the amount of adsorbed phenol species decreased. This decrease in the adsorption capacity is related to the affinity of water for the aluminum atoms. Comparison of the performances of different zeolites showed that hydrophobic zeolites with high Si/Al ratio are recommended for a selective and reversible adsorption of phenol into aqueous phase.[16] For the same purpose, Roostaei et al.[19] have tested alumina and silica gel but their results showed no significant adsorption of phenol into water over these solids. In contrast, over a Y-type zeolite, the kinetics of adsorption was fast and reversible and the phenol diffusion increased for small particle sizes.[19] At the end, both studies have shown that charcoal presents the highest adsorption capacity but due to its high price and its regeneration cost it cannot be used as an adsorbent at an industrial scale[16,19,20].

In contrast, only a very few studies have dealt with the elimination of phenol-derivatives from hydrocarbons. Two patents published in 1952 and 1971 studied phenol removal from hydrocarbons. [21,22] The first patent proposed a treatment of the phenol containing stocks with a strong alkali metal hydroxide solution. The second patent proposed to adsorb phenol over polyurethane foams followed by regeneration with acetone. These two processes are far from the requirement of green chemistry and alternative adsorption solutions are still required. In this context, we propose to test the promises of a series of protonated Y zeolites for the elimination of phenol from a hydrocarbon mixture by adsorption. Their performances are assessed terms of adsorption capacities and regenerability of the materials. In particular, the influence of the Si/Al ratio (from 2.5 to 47) was studied through a combination of breakthrough curves experiments, characterization of materials and molecular simulation techniques.

The paper is organized as follows: in Section 2, the experimental and computational methods are presented. In Section 3, after a complete characterization of the zeolitic solids, the experimental results

regarding the adsorption capacities of HY and various USY are discussed in light of our Grand Canonical Monte Carlo (GCMC) simulations. The regeneration and recycling abilities of the investigated zeolites are further assessed by desorption experiments and completed by the evaluation of the adsorption energies computed by Density Functional Theory (DFT) calculations. Finally, we will give our conclusions in the last section.

2. Methods

2.1 Characterizations of the adsorbents

Y zeolite with Si/Al ratio of 2.5 was supplied by Union Carbide. Ultra stable Y (USY) zeolites with Si/Al ratios varying from 13 to 40 were supplied by Zeolyst International. The chemical composition of zeolites was checked by inductively coupled plasma (ICP) coupled with optical emission spectroscopy using a Varian ICP-OES 720-ES. Their textural properties were characterized by nitrogen adsorption isotherms at 77K using gas adsorption system ASAP 2020 (Micrometrics) for a relative pressure (P/P_0) between 0.05 and 1. Total and external surface areas were determined using the t-plot method.

X-ray powder diffraction (XRPD) patterns were obtained with a PANalytical X'Pert PRO diffractometer with Cu Kα radiation (λ= 0.15418 nm, 40 mA, 45 kV, the step size of 0.02° and a scan speed of 1° min^{-1}). By using X'Pert Highscore plus software we can determine the lattice parameter of the different zeolites. This parameter allows the estimation of the number of aluminum atoms per unit cell of the zeolite framework (N_{Al}) by applying the formula quoted in Table SI-1.[23] The degree of crystallinity of the zeolite fraction can be calculated by comparing the sum of the areas of the four most intense Bragg diffraction peaks at 2θ of 20.4°, 23.7°, 27.1° and 31.4° of the considered sample with the sum of the same peak areas of the HY2.5 zeolite that is considered as a fully crystalline zeolite[24].

^{29}Si MAS NMR and ^{27}Al MAS NMR spectra were recorded on a Bruker Avance III 500 MHz (11.7 T) spectrometer. 4 mm rotor and a spinning speed of 12 kHz, for silicon, and 14 kHz for aluminum, were

used. For ^{29}Si MAS NMR, spectra were measured at a Larmor frequency of 79.4 MHz, with a 30° pulse and a recycle delay of 20s. For ^{27}Al MAS NMR, measurements were carried out at 130.3 MHz, with a 10° selective pulse and a recycle delay of 1s. Tetramethylsilane (TMS) and $Al(NO_3)_3$ (1M) were used as references for ^{29}Si and ^{27}Al, respectively. ^{27}Al-NMR was used to determine the ratio between framework aluminum atoms (Al(IV)) and extra-framework aluminum atoms (Al(VI) and Al(V)) while ^{29}Si-NMR served to determine the degree of crystallinity for USY13 and USY33 adsorbents. The crystallinity was calculated by comparing the sum of the areas of the signals specific of the Si atoms in close connection with 1, 2 or 3 Al atoms to the total area of the Si atom signals.

The acidic sites characterization was performed by pyridine adsorption followed by infrared (IR) spectroscopy. Each sample was pressed into a self-supported wafer (10-15mg, precisely weighted) with a surface of 2 cm^2 under a pressure of 10^7 Pa. Sample wafer was then activated by heating from 298 K to 623 K ($1K.min^{-1}$) followed by an isotherm at 623 K for 4 hours under secondary vacuum (10^{-4} Pa). The vapor of pyridine was introduced into the cell at RT with calibrated doses from 0.05 to 1.70 µmol. A final equilibrium pressure of 266 Pa was established in the IR cell. Desorption was carried under secondary vacuum from room temperature (RT) up to 423 K for 20 minutes at each temperature. The FTIR spectrometer was a Thermo Fischer 6700 equipped with an MCT detector. 64 scans were accumulated for each measurement with a resolution of 4 cm^{-1}. Spectra were analyzed by calculating the difference between spectrum after pyridine adsorption (or desorption) minus spectrum corresponding to the activated sample. All spectra were normalized to a disc constant mass (5 $mg.cm^{-2}$ of dried catalyst).

2.2 Phenol adsorption experiments

Phenol adsorption experiments were performed under flow conditions. Phenol (Aldrich, 99.5% purity) was used as a model molecule for all the adsorption studies. The liquid solution containing phenol was obtained by dissolving 7.0 g (1 wt.%) of phenol into 1000 mL of isooctane (Aldrich, 99+% purity). The amount of phenol in the solution was chosen by taking into consideration the quantity of phenol

present in biofuels after FCC treatment as well as the limit of solubility of phenol in isooctane (2.5 wt.%). Adsorption experiments were performed at room temperature and atmospheric pressure.

For all these experiments, adsorbents were activated by an *in-situ* pretreatment at 623K for 4 hours under argon flow to obtain the protonic form of the zeolites and to remove adsorbed water from the pores. Adsorption tests were performed in a glass column with a length of 300 mm and an internal diameter of 6 mm. 0.5 g of zeolites, with a granulometry between 200 and 400 µm, is packed which gives a bed volume from 2 to 3 cm^3. The phenol in isooctane solution was fed into the column using a Gilson pump allowing a constant flow rate of 1 $ml.min^{-1}$. The solution was collected periodically and analyzed by a Shimadzu 2010 gas chromatograph with a CP-sil 5CB capillary column (30 m), using a flame ionization detector and nitrogen as a carrier gas. The results were obtained as a breakthrough curve and the amount of phenol adsorbed per gram of solid was calculated using the following equation (1):

$$q = \frac{C_0.D.t_R}{m_{ads}} \qquad (1)$$

where q is the amount of adsorbed phenol by gram of solid ($mmol.g^{-1}$), C_0 is the initial phenol concentration ($mmol.L^{-1}$), D is the flow rate of the charge containing phenol ($L.min^{-1}$), m_{ads} is the mass of zeolite (g), and t_R is the retention time (min) when the ratio of C_t/C_0 is equal to 0.5.

The adsorbent capacity to perform several adsorption cycles was also tested. After one cycle, the adsorbent was *in situ* regenerated under mild conditions i.e. by an argon flow (90 $cm^3.min^{-1}$) at 473 K for 4 hours. Successively, a second adsorption was performed under the same condition as the first cycle.

2.3 Computational methods

2.3.1 Force-field-based Grand Canonical Monte Carlo

Force-field-based GCMC simulations were performed to explore the single component adsorption behavior of the phenol into a series of faujasites at T=300 K using the CADSS simulation code.[17] The

simulation box consisted of one faujasite unit cell considering crystal models for DAY, USY and HY described in Section 2.3.3. The interactions between phenol and the faujasites were described by a combination of a Lennard–Jones (LJ) potential van der Waals term and a Coulombic contribution. The LJ force field parameters for all zeolite atoms were taken from the TraPPE-Zeo force field parameterized by Bai *et al.*[25] which has been proved to accurately predict both adsorption and diffusion of hydrocarbons and oxygenated molecules over a wide range of pressures and temperatures in zeolites.[25]

The partial charges for each atom of the faujasites were those derived by Jousse et al.[26] The phenol molecule was described by the TraPPE potential model,[17,25,27] that was derived using the vapor-liquid equilibrium (VLE) data.[28] The whole set of potential parameters and charges is summarized in (Table SI-2). The cross-interaction LJ parameters to describe the phenol/faujasite interactions were obtained using the Lorentz-Berthelot mixing rules.[29,30] A cutoff radius of 12.0 Å was applied to the LJ interactions, while the long-range electrostatic interactions were handled by the Ewald summation technique. For each state point, GCMC simulations consisted of 2.10^7 steps to ensure the equilibration, followed by 5.10^7 steps to sample the desired thermodynamic properties. For the simulations, a configurational-based GCMC scheme was considered with four types of trials: (i) displacement of a molecule (translation or rotation), (ii) a partial and full regrow of a molecule, (iii) creation of a new molecule and, (iv) deletion of a molecule. The adsorption enthalpies were calculated using the revised Widom's test particle method.[31] NVT Monte Carlo simulations were run at different loadings to calculate the radial distribution functions (RDFs) between the phenol and the faujasites and to gain insight into the adsorption mechanism.

2.3.2 Density Functional Theory

DFT calculations have been performed using the Vienna *Ab initio* Simulation Package (VASP).[32–35] These calculations employed the PBE functional and the PAW method developed by Blöchl as adapted by Kresse and Joubert,[36,37,38] a plane-wave cutoff energy of 450 eV and a Gaussian smearing of 0.1 eV. The Kohn–Sham equations were solved self-consistently until the inter-cycles energy

difference takes a value smaller than 10^{-6} eV. The structural relaxations have been carried out until all forces were smaller than 0.02 eV/Å. The Brillouin zone sampling was restricted to the Γ-point. To take into account the van der Waals interactions which are not correctly treated by the PBE functional, we have selected two correction methods: (1) the semi-empirical scheme D2 reported by Grimme where the C_6 coefficients are tabulated,[39] and (2) the more sophisticated FI/MBD correction which considers many-body interactions, [40,41,39] ionicity of the atom and C_6 coefficients which depend on the electronic density. These methods have been implemented in VASP and tested for different systems by Bučko et al.[40,42,43] These methods have been demonstrated to describe accurately the adsorption of molecules into zeolites.[44–46] The phenol/faujasite interaction energy (ΔE_{int}) was calculated using the following equation:

$$\Delta E_{int} = E_{zeolite-phenol} - E_{zeolite} - E_{phenol} \qquad (2)$$

Where $E_{zeolite\text{-}phenol}$: the energy of the zeolite with the phenol adsorbed inside; $E_{zeolite}$: the energy of the empty zeolite and E_{phenol}: the energy of the isolated phenol in the gas phase.

The contribution of the dispersion (ΔE_{disp}) to the interaction energy was estimated as follows:

$$\Delta E_{disp} = E_{disp\ zeolite-phenol} - E_{disp\ zeolite} - E_{disp\ phenol} \qquad (3)$$

Where $E_{disp\ zeolite\text{-}phenol}$: the dispersion energy of the phenol loaded into the zeolite; $E_{disp\ zeolite}$: the dispersion energy of the empty zeolite; $E_{disp\ phenol}$: the dispersion energy of the isolated phenol in the gas phase.

2.3.3 Structural models of faujasite

Three faujasites with different Si/Al ratios have been considered to model the different investigated samples.

- A pure siliceous faujasite named as DAY was used to simulate the siliceous supercages which are presents in USY with high Si/Al ratios.[47,48]

- The USY model (Si/Al = 47) was built by substituting a Si atom by an Al atom and adding one H atom on one neighbor O atom in the 6MR window to investigate an isolated Brønsted acid site. A Lewis acid site (LAS) can be similarly modeled just by deleting the H atom from the USY model.
- The HY (Si/Al = 2.5) was represented by the model previously reported by Sastre *et* al.[49] which was built by confrontate periodic DFT modeling with IR spectroscopy to mimic realistic HY zeolites

These structures were considered in their primitive rhombohedral and conventional cubic cells (see Table SI-2). The primitive cell that contains two supercages and eight hexagonal windows connecting the sodalite with these supercages was used for DFT calculations. The conventional cell that contains 8 supercages was employed for the GCMC simulations.

These three models of primitive cells were preliminary fully optimized (position of atoms, cell shape and cell volume relaxed) at the PBE+D2 level of theory to use these structures by GCMC simulations, we have converted the optimized unit primitive cells to the corresponding conventional unit cells (see Table SI-2 and Figure SI-1 for details).

3. Results and discussion

3.1 Adsorbents characteristics

The structural and textural properties of the various adsorbents are presented in Tables SI-1 and SI-4. Table SI-4 shows that the total surface area of HY2.5 (1063 $m^2.g^{-1}$) is clearly larger than that of USY samples (~930 $m^2.g^{-1}$), while the external surface area of the dealuminated zeolites (up to 112 $m^2.g^{-1}$) is larger than that of the HY2.5 zeolite (49 $m^2.g^{-1}$). Hence, the extent of dealumination tends to increase the external surface area. We observed that the total pore volume is higher for USY (~0.50 $cm^3.g^{-1}$) compared to HY zeolite (0.39 $cm^3.g^{-1}$). By contrast, the micropore volume is slightly smaller for USY zeolite (~0.30 $cm^3.g^{-1}$) than for the parent one (0.36 $cm^3.g^{-1}$). These results are consistent with the fact that the dealumination usually leads to a partial destruction of the crystalline microporous network and to the formation of new large pores in the zeolite crystal.[50]

Table 1 – Chemical formula of the different adsorbents

Adsorbents	Formula [a]	Si/Al[b] Framework	nAl (mmol.g^{-1})		
			Total	Framework	EFAL
HY2.5	$M_{54.8}\,(AlO_2)_{54.8}\,(SiO_2)_{137.2}$	2.5	4.25	4.25	0
USY13	$M_{12.5}(AlO_2)_{12.5}(SiO_2)_{179.5}$; $2.9(Al_2O_3)\ 59(SiO_2)$	14	1.19	0.81	0.38
USY22	$M_{7.1}(AlO_2)_{7.1}(SiO_2)_{184.9}$; $2.1(Al_2O_3)\ 64(SiO_2)$	26	0.72	0.46	0.26
USY33	$M_{5.5}(AlO_2)_{5.5}(SiO_2)_{186.5}$; $2.1(Al_2O_3)\ 130(SiO_2)$	34	0.49	0.28	0.21
USY40	$M_{3.7}(AlO_2)_{3.7}(SiO_2)_{188.3}$; $1.8(Al_2O_3)\ 100(SiO_2)$	51	0.41	0.21	0.20

[a] Atomic ratio determined by combining data from ICP, ^{27}Al-NMR, ^{29}Si-NMR and XRD analysis.
[b] Based on the values of the chemical formula in the table.

XRPD, ^{27}Al NMR and ^{29}Si NMR data (Figure SI-2) allowed the estimation of the Si/Al ratio and the crystallinity of the zeolite (Table SI-1). As shown in Table SI-5, the crystallinity values determined by the two approaches are very close. In the following calculations, Si/Al ratios issued from ^{27}Al NMR and crystallinity values issued from XRPD will be considered.

By combining the data issued from ICP, XRPD, ^{27}Al-NMR, and ^{29}Si-NMR, the complete formula of each adsorbent can be determined (SI section 4). The formula presented in Table 1 are expressed as $M_x\,(AlO_2)_x\,(SiO_2)_y$; $z(Al_2O_3)\ t(SiO_2)$ where x and y correspond to the number of Al and Si atoms in the zeolite framework respectively, z and t correspond respectively to the number of extra-framework Al (EFAL) and Si atoms of the zeolite and finally M represents the counter cation. The counter cations of these samples are not only protons but they can be also Na^+ (seen by the ICP analysis), NH_4^+ (from ^{1}H-NMR, results obtained after the solids pretreatment) as well as Al^{3+} in the USY samples as demonstrated by Malicki *et al.*[51] The ratio between the different cation forms varies according to the sample.

The acidic properties of the adsorbents were characterized directly by the quantification of the zeolitic ν(OH) bands at 3640 and 3545 cm^{-1} (Figure SI-3 and Table 2) and indirectly by pyridine adsorption (Figure SI-4).[52,53] Indeed, in the IR spectra recorded after the pyridine adsorption, the band at 1545 cm^{-1} is characteristic for pyridinium ions PyH^+, and that at 1455 cm^{-1} reveals to coordinated pyridine (LPy). The densities of Brønsted (BAS) and Lewis (LAS) acid sites can thus be deduced from their integrated intensities (ε(PyH^+) = 1.8 µmol^{-1}.cm; ε(LPy) = 1.5 µmol^{-1}.cm).[54] As shown in Table 2, all

the samples present Brønsted acid sites (BAS) and Lewis acid sites (LAS) in very different amounts and ratios.

Over HY2.5 zeolite, the amount of OH located in the supercages is consistent with the PyH^+ species. This is related to the steric hindrance of pyridine, since pyridinium ions are formed from the interactions with the OH groups present in the supercages and not the ones in the sodalite cages. By contrast and as already observed on dealuminated zeolites, pyridine is able to form pyridinium ions with the OH groups of the supercage, the OH groups of the sodalite cages (due to the mobility related to their strongly acidic character) as well as the OH groups of the extraframework amorphous silica alumina phase (ASA).[52,55]

Table 2 – Brønsted and Lewis acidic sites concentration as determined by pyridine adsorption. Amount of Brønsted acid site versus the amount of OH groups in the zeolitic framework.

Adsorbents	Amount of OH supercage* ($\mu mol.g^{-1}$)	Amount of OH sodalite* ($\mu mol.g^{-1}$)	Acid sites ($\mu mol.g^{-1}$)		
			BAS	LAS	Total
HY2.5	1160	2040	1263	22	1285
USY13	51	68	321	211	532
USY22	45	58	136	189	325
USY33	30	22	101	62	163
USY40	22	25	60	17	77

*molar absorption coefficients: $\varepsilon(\nu_{OH\ supercage}) = 7.5\ \mu mol^{-1}.cm$; $\varepsilon(\nu_{OH\ sodalite\ cage}) = 5.6\ \mu mol^{-1}.cm$[52]

3.2 Phenol adsorption capacities

3.2.1 Breakthrough curves

We have first noticed that isooctane is not retained by any zeolite considered in this work. The breakthrough curves obtained for the adsorption of phenol in isooctane ($7g.L^{-1}$) over the different adsorbents are shown in Figure 1. Overall the adsorbents, the retention time is similar varying from 13 to 15 min. The maximum amount of phenol adsorbed per gram of adsorbent at this retention time was calculated according to equation (1). For all the studied zeolites, the maximum adsorption capacity varies between 2.0 and 2.2 $mmol.g^{-1}$ (Figure 1). Consequently it appears that the Si/Al ratio is not the factor that determines the maximum adsorption capacity of phenol in a hydrocarbon mixture. Our

results contrast with what is observed for phenol adsorption from aqueous solution, where a high Si/Al ratio was recommended to limit the water adsorption and increase the amount of adsorbed phenol species.[16] We should mention that, in this work, the maximum adsorption capacity over HFAU (2.2 mmol.g^{-1}) is higher than that obtained in previous work dealing with the phenol adsorption from wastewater (~ 0.5 mmol.g^{-1}).[16] This difference is related to the higher initial concentration of phenol in the solution (7 g.L^{-1} in our study for 0.8 g.L^{-1} in the previous work) and also to the different type of the used solvent, since that with isooctane we are less bothered by the competitive adsorption.

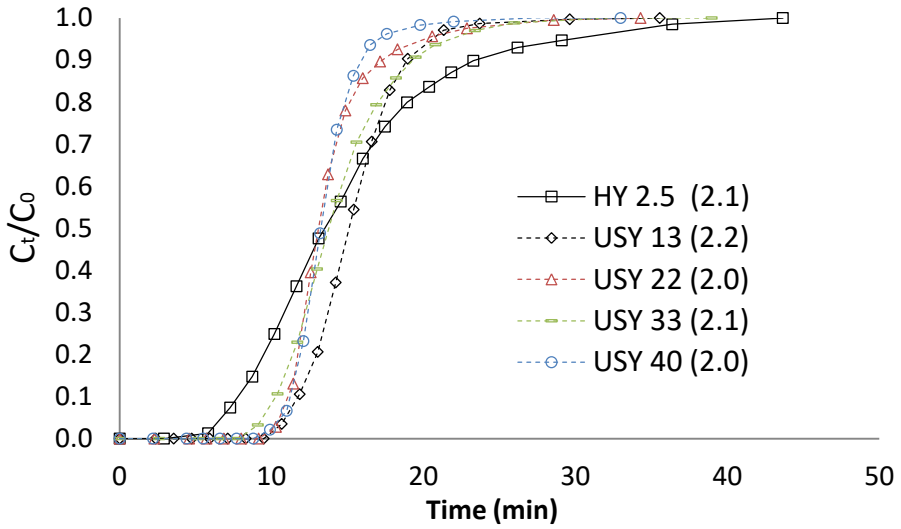

Figure 1: Breakthrough curves of phenol adsorption over the studied zeolites In parenthesis: the amount of adsorbed phenol at retention time in mmol.g^{-1}

The maximum adsorption capacity is not the only key factor to select the most efficient adsorbent. Since we are looking to obtain ultra pure biofuel, we have to avoid any release of phenol during the adsorption process. In this respect the most efficient adsorbent will be the one which present the latest breakthrough time. It can be seen in the Figure 1 that the slope of the breakthrough curve for HY2.5 (solid line) is very smooth compared to the ones obtained for the USY series (dashed lines). Indeed, on HY2.5, the breakthrough is detected after 6 min of adsorption but the solid is saturated by phenol 45 min later. For all the dealuminated zeolites, the breakthrough occurs after almost 10 min, and the adsorbents reach a total saturation in 8 to 10 min later. Hence after the breakthrough, the USY-type adsorbents are quickly saturated by phenol. On these dealuminated zeolites, the creation of large pores at the expense of microporosity as well as the low density of acidic sites facilitates the phenol

diffusion. In contrast, for the HY2.5 zeolite, the large amount of acidic sites available as well as its microporous-type of porosity makes the phenol diffusion slower than for USY zeolites. As a conclusion, USY40 appears as the best candidate to efficiently remove phenol from an isooctane solution.

3.2.2 Determination of the amount of phenol molecules per zeolitic supercage

In this section we will consider the effects of textural and structural properties of the various adsorbents on their phenol adsorption capacity.

As for textural properties, adsorption capacities of the studied samples cannot be related to the surface area. Indeed, HY and USY possess similar phenol adsorption capacities whereas their surface areas are very different (Table SI-4). The studied adsorbents present similar total pore volume but with different distributions of the pores sizes. The size of the phenol molecule (kinetic diameter = 0.56 nm[56]) allows its easy entrance in the supercage of the HY2.5 network (supercage aperture = 0.74 nm ; supercage internal diameter = 1.30 nm[57,58]) but not in the sodalite cage (aperture = 0.25 nm[57]). Moreover for USY samples, the dealumination creates large pores in the amorphous zone (greater or equal to the size of a supercage) in which phenol molecules can be obviously adsorbed.

We further wanted to determine how much phenol molecules can be adsorbed into one faujasite supercage. The amount of phenol species adsorbed into the micropores of the zeolite crystalline form (N_{ph}) can be assessed considering the ratio between the micropore volume and the total pore volume (Table 3). Moreover, considering the crystallinity of the USY zeolite and since a fully crystalline faujasite possesses 4.2 x 10^{20} cages per gram,[59] it is possible to calculate, for each adsorbent, its number of supercages per gram (N_{SC}). Dividing the number of phenol molecules into the micropores per the number of present supercages in each gram of solid, the number of phenol molecules per supercage for the different adsorbents can be obtained.

Table 3 shows that the number of phenol molecules per supercage of the faujasite is almost constant and close to 3 whatever the zeolite considered. Indeed, the number of phenol molecules per supercage varies between 2.4 and 3.0 for the various studied zeolites.

Table 3 –Phenol molecules adsorbed in the adsorbent and into the zeolite framework. Number of phenol molecule per supercage of the zeolite (N_{ph} / N_{sc})

Adsorbents	Adsorbed phenol ($mmol.g^{-1}$)	% of micropores [a]	N_{ph} in micropores per g of solid N_{ph} [b] ($*10^{20}$)	N_{SC} in the crystalline form per g of solid N_{sc} [c] ($*10^{20}$)	N_{ph} / N_{sc}
HY2.5	2.1	92	11.7	4.2	2.8
USY13	2.2	69	9.1	3.2	2.9
USY22	2.0	61	7.3	3.1	2.4
USY33	2.1	60	7.5	2.5	3.0
USY40	2.0	60	7.2	2.7	2.7

[a] (micropore volume) / (total pore volume)
[b] N_{ph} = (adsorbed phenol molecules) x (% of micropores)
[c] N_{sc} = ($4.2*10^{20}$supercages) x (crystallinity)

3.2.3 GCMC simulations

The simulated adsorption isotherms for the three faujasites are reported in Figure 2. It is shown that at saturation pressure, all the zeolites have the same phenol uptake of 32 molecules per conventional unit cell, i.e. 4 molecules per supercage. This value is slightly higher than that obtained in the experimental study. We can provide two comments to explain this difference: first, our theoretical adsorption capacity corresponds to a system saturated by phenol whereas the experimental phenol concentration in the liquid feed during the breakthrough curve experiments is below the saturation limit. The difference can be also related to the limitation of the phenol diffusion in zeolites pores due to the presence of defects or external surfaces which are not taken into account in our models.

Figure 2 shows that at low pressure, the adsorption isotherms show distinct slopes for the three faujasites. This trend reflects a different affinity for the phenol and the role of the protonated sites at the initial stage of adsorption. This result is consistent with the experimental observation reported by the breakthrough curves of Figure 1.

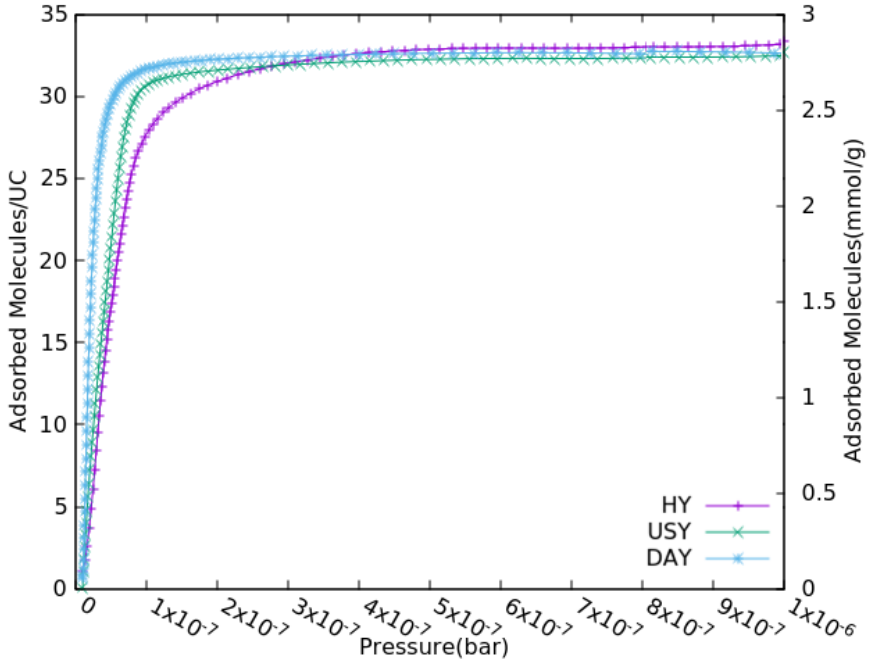

Figure 2: GCMC simulated adsorption isotherms for phenol in HY (purple dotted line), USY (green dotted line) and DAY (blue dotted line) at 300 K

Figure 3 reports the simulated adsorption enthalpy profile as a function of the amount of adsorbed phenol. At low loading, the adsorption enthalpies of phenol in DAY, USY, and HY are around -79, -81, and -83 kJ/mol respectively. So, the adsorption enthalpy increases with the amount of Brønsted acid sites present in the material, meaning that the presence of the bridging hydroxyl group Al-OH-Si enhances the strength of interactions between the zeolite and the phenol. Furthermore, we observed that the adsorption enthalpy increases with the phenol loading due to the increase of the phenol/phenol interactions.

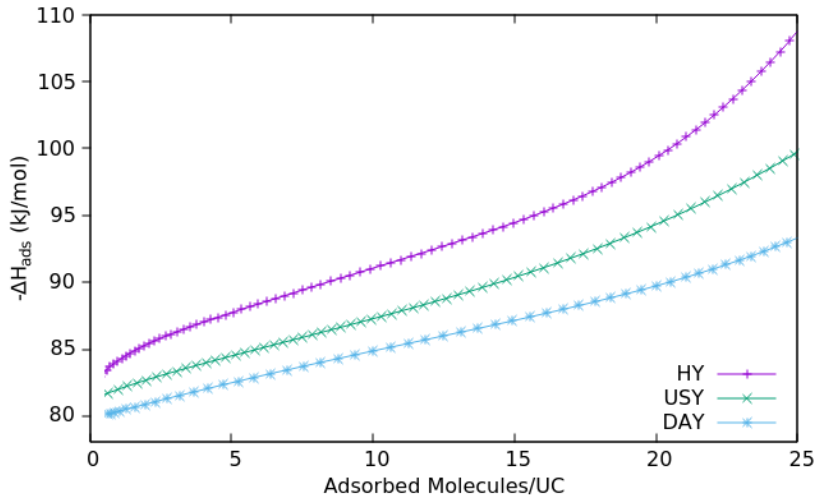

Figure 3: Adsorption enthalpy of phenol adsorbed into HY (purple dotted line), USY (green dotted lines) and DAY (blue dotted line) versus adsorbed molecules.

As a further step, the preferential adsorption sites of phenol were explored. We first observed that, at the initial stage of adsorption, the interactions between phenol and DAY occur between the hydrogen atoms of the hydroxyl function of phenol and the oxygen atoms of DAY with a characteristic distance of about 2.5 Å as shown in the corresponding radial distribution functions and snapshot on the right-hand side (Figure 4a). In the case of the protonated faujasites USY and HY, the most probable interactions take place between the oxygen atom of the hydroxyl function of the phenol and the hydrogen atom of the bridging hydroxyl group Al-OH-Si of the protonated faujasites, with a characteristic distance of about 2.5 Å (Figure 4b and c). This emphasizes the predominant role of the O_{phenol}-$H_{zeolite}$ interactions in the adsorption of phenol in USY and HY zeolites. These predominant interactions are illustrated by the snapshots reported in Figure 4(a-c).

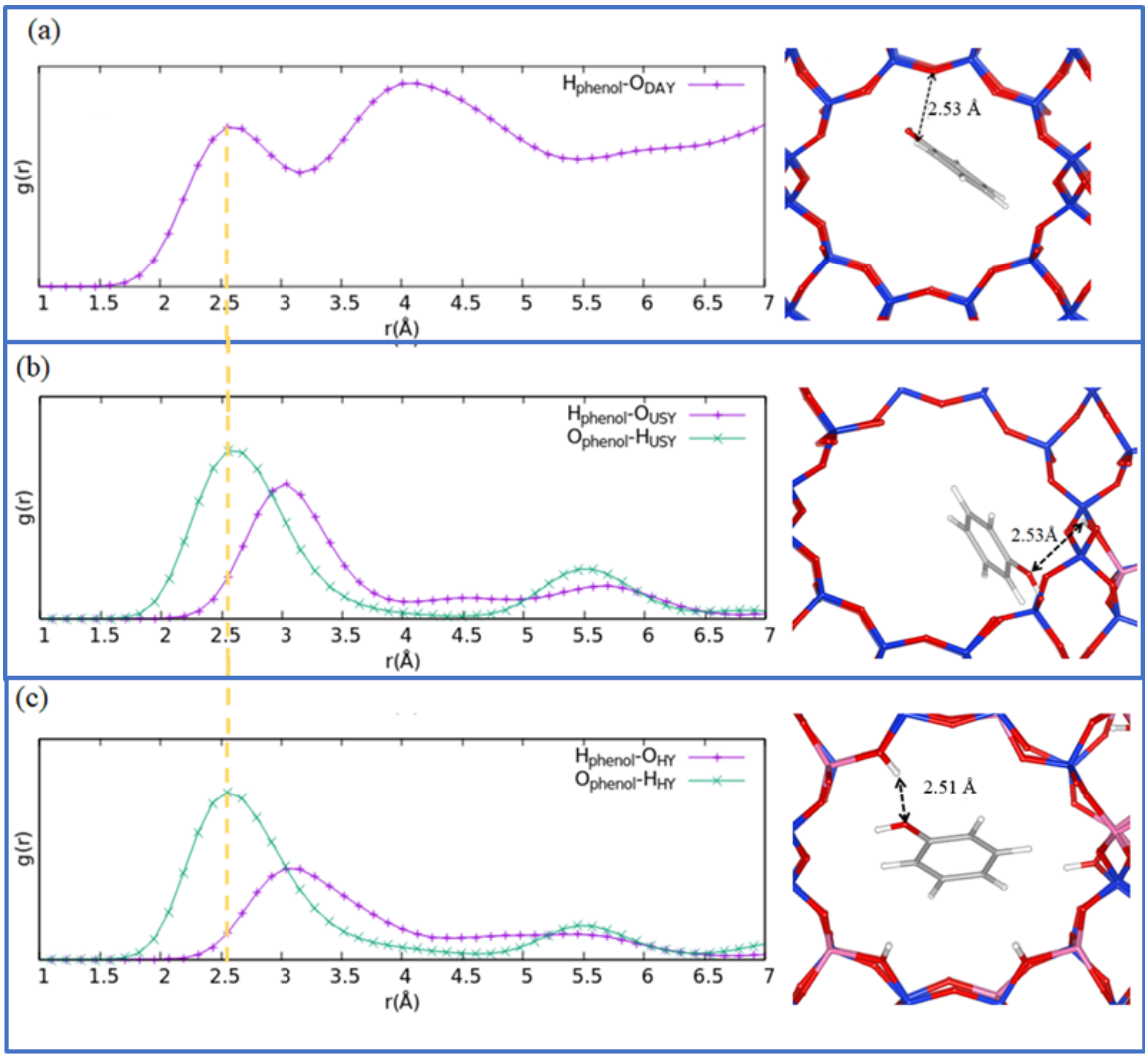

Figure 4: GCMC simulation of the phenol location at low phenol loading in (a) DAY, (b) USY, (c) HY. Purple curves represent $O_{Network}$ –H_{phenol} correlations. Green curves represent $H_{Network}$–O_{phenol}. Right-hand side: Snapshot of the phenol adsorbed in the faujasite supercage, pink knots = Al, blue knots = Si, red knots = O, gray knots = C, whiteheads = H atoms

We further evidenced at high coverage a OH- π type interaction. This is consistent with the previous work reported by Jentys et al.[60] who revealed that the adsorption of the aromatic molecule on the MCM-22 zeolite involved the interactions between the electrons π of the aromatic molecule and the silanol terminal group Si-OH. The computed preferential distribution of phenol molecules at saturation is presented in Figure 5. We evidenced that the phenol molecules are randomly distributed in the 12MR channels of all faujasites. In the case of DAY, the phenol molecules are found to form agglomerates of four molecules per supercage (Figure 5a). We can notice that the shape of these phenol clusters is the same from one supercage to another throughout the DAY.

In the USY, the phenol molecules are also homogenously agglomerated in the differently modeled supercages. A slight difference in the geometry is shown when comparing with DAY cages, which is due to the phenol interaction with the Brønsted acid site of the USY supercage (Figure 5b). These guest molecules mostly interact together via hydrogen bonds between the hydroxyl groups of two consecutive molecules with short characteristic distances H(OH)-O(OH) ~2Å (see Figure SI-5). This is even more pronounced for DAY and USY as shown by a higher intensity of the corresponding peak present in the RDFs.

In the HY, the phenol agglomerations are not perfectly spherical as observed in both DAY and USY, due to the presence of a high number of π –stacked phenols (see the 3 upper stacked-molecules in Figure 5c).

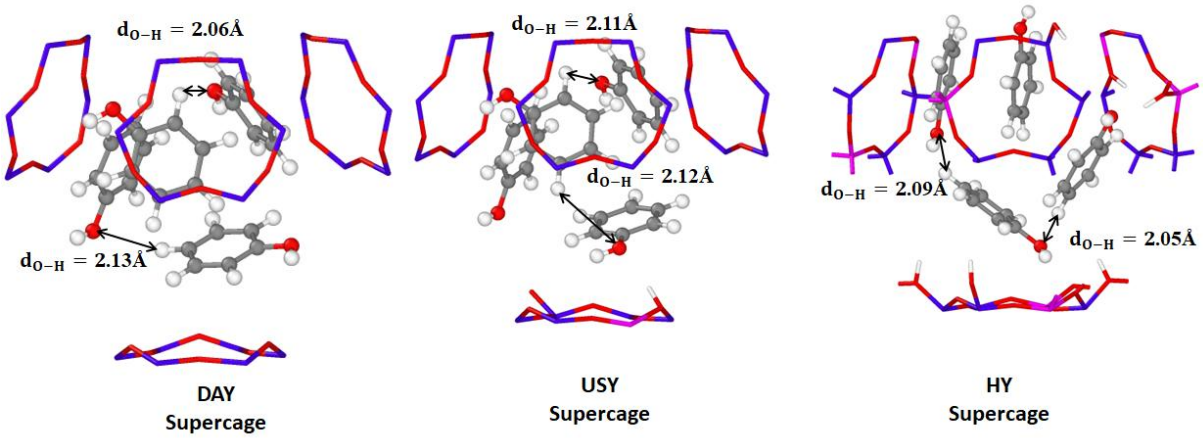

Figure 5: Simulation of the preferential arrangements of phenol confinements inside a supercage of (a) DAY, (b) USY and (c) HY. Red knots = O atoms; gray knots = C atoms, white knots = H atoms.

3.3 Regeneration of the adsorbents

3.3.1 Residual phenol species

As mentioned in the introduction, when using an adsorption process for the purification of a mixture, an important parameter that will determine the choice of the adsorbents is the regeneration and recycling properties.[15,16] In the present study, after one cycle of phenol adsorption, the ability of the various zeolites to be regenerated under mild conditions was tested through the determination of

adsorption capacities in a second cycle. To remove the adsorbed phenol molecules, a thermal treatment under Argon flow (90 $cm^3.min^{-1}$) at 473 K for 4 hours was applied. Note that phenol crystallized at the outlet of the experimental device due to the condensation of phenol species in the line. The analysis of these crystals by IR-ATR confirmed the condensation of phenol without any chemical transformation. The performances after two adsorption-desorption cycles and the regeneration ability of each solid is shown in Table 4.

Table 4 – Capacity of the zeolites for phenol adsorption and regeneration over two cycles.

Adsorbents	Adsorbed phenol ($mmol.g^{-1}$)		Residual phenol ($\mu mol.g^{-1}$)	Regeneration capacity (%)
	Cycle 1	Cycle 2		
HY2.5	2.1	0.9	1200	43%
USY13	2.2	1.6	600	73%
USY22	2.0	1.6	350	83%
USY33	2.1	1.9	150	93%
USY40	2.0	1.9	100	95%

Analysis of these results showed that the amount of adsorbed phenol in cycle 2 increases with the Si/Al ratio of the zeolite (Table 4). Hence, dealumination clearly improves the regeneration capacity of the zeolitic adsorbent. Indeed it reaches 43% on HY2.5 whereas it increases up to 95% on USY33 and USY40.

3.3.2 Residual phenol species as a function of the acidic properties

To identify the nature of the sites responsible of the residual phenol species formation (species non-desorbed after Argon flush at 473K), a parallel between the amount of these residual phenols species and the acidic properties of the adsorbents has been made. The amount of residual phenol species were compared to the different acid sites concentration of the adsorbent. Figure SI-6 reports the residual species amount versus the concentration of LAS or BAS, while Figure 6 presents a comparison with the total amount of acid sites. The best fitting was obtained when the presence of both BAS and LAS was considered (R^2 = 0.986). Hence, strongly adsorbed phenol species can be formed on the zeolitic proton as well as on the extraframework LAS sites of the adsorbent. From these results, one can

conclude that decreasing the acidic properties of the adsorbent is an efficient way to improve the regeneration capacity. Figure 6 points out that, for HY2.5 zeolite that presents mainly BAS, almost 1200 µmol of residual phenol molecules remain in high interaction with 1285 µmol of total acid sites, moreover the slop of the curve gives a value near to 1 which confirms that over one acid site only one residual phenol molecule can be strongly adsorbed.

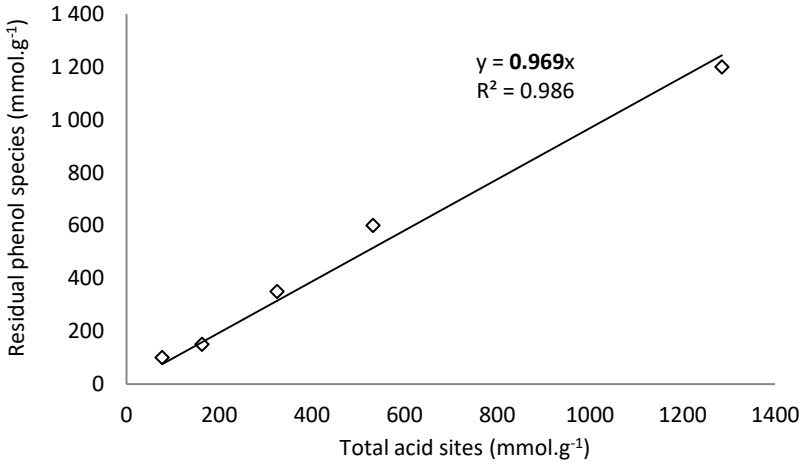

Figure 6: Amount of residual phenol as a function of acid sites in USY zeolites

3.3.3 Interaction energies of phenol over DAY, USY and HY

Using periodic DFT calculations, the interaction energies of isolated phenol molecule on the different models representative of the different zeolites were computed (Figure 7). The supercages can contain BAS, LAS or can be purely siliceous; the probability of the presence of these 3 supercage types mainly depends on the Si/Al ratio. The interaction energy of phenol with the different supercage types was calculated using two dispersive-corrective methods, D2 and FI/MBD (Table 5), which led to similar results. In the DAY supercage, phenol accommodates in a parallel plane to the 6MR window with interaction energy of -51 kJ.mol^{-1} (Figure 7 and Table 5). The adsorption of phenol in the protonated faujasites may involve a donor-electron acceptor complex without ignoring the presence of dispersion forces between the π-electrons of the phenol and the proton of the bridging hydroxyl group Al-OH-Si. In presence of an isolated Brønsted acid site in the supercage (USY model with Si/Al=47),

the interaction energy of phenol increases to -85 kJ.mol^{-1}. On HY zeolites (Si/Al = 2.5) the interaction energy of the phenol with one zeolitic proton reaches -94 kJ.mol^{-1}. Note that this sample does not present any Lewis acid sites. Compared to an isolated Brønsted site (-85 kJ.mol^{-1}), phenol adsorbed in HY zeolite presents a slightly higher interaction energy by around 10 kJ.mol^{-1}.

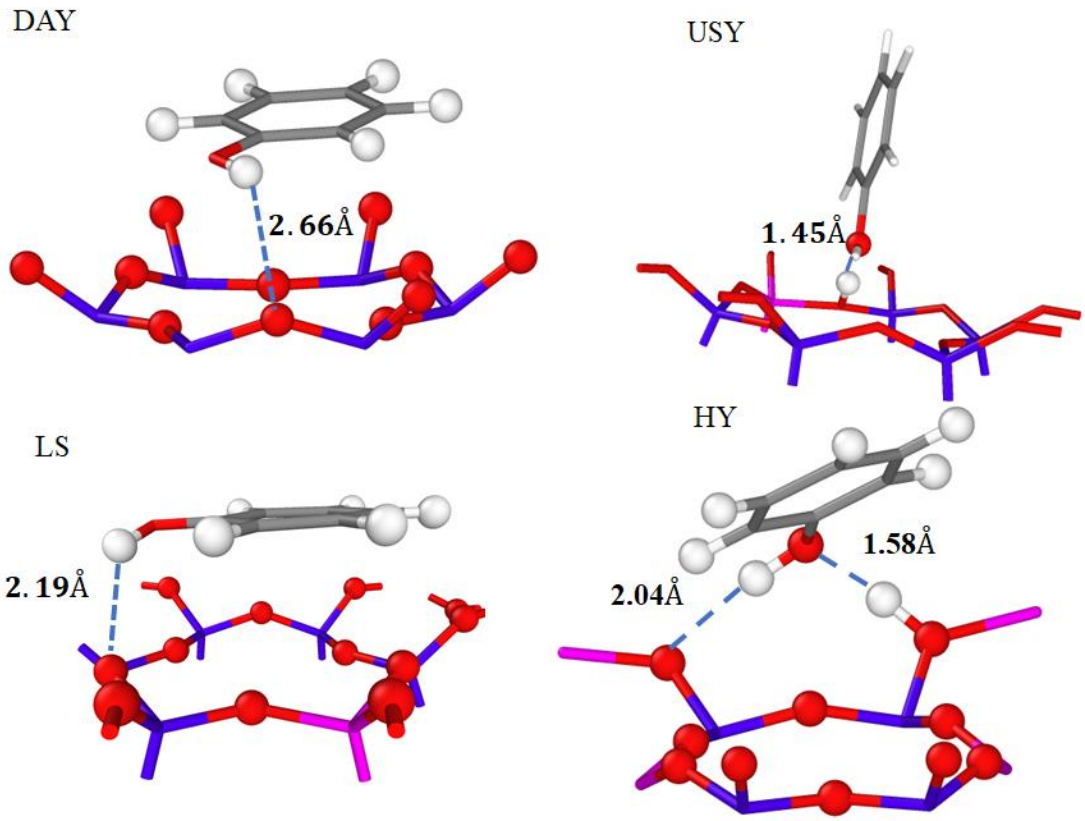

Figure 7: Configuration of one isolated phenol molecule adsorbed into DAY, USY, LS and HY supercages computed by DFT calculation at 0 K.

These DFT-interaction energies are consistent with those simulated by GCMC simulations (section 3.2.3). This observation suggests that both microscopic models used to represent the zeolites and the phenol, as well as the cross interatomic LJ contributions, are accurate enough to account well the adsorption process. Over a Lewis acid site, the interaction energy is much higher and goes up to -154 kJ.mol^{-1}. We have noticed that the phenol molecule prefers the O-interaction over a Brønsted acid site and the π-interaction over a Lewis acid site. We also observed that phenol interacts with one Brønsted site in our USY and HY models, which is consistent with the slope of the curve presented in Figure 6.

Table 5 – Interaction energy (dispersion energy) calculated by two different methods for phenol into faujasites: DAY (pure siliceous), USY (1 acidic proton every two supercages and 1 LAS every two supercages) and HY (only acidic proton)

	ΔE_{int} (ΔE_{dis}) in kJ.mol^{-1}	
vdW correction methods	D2	FI/MBD
DAY	-51 (-46)	-49 (-39)
USY/Interaction with one acidic proton	-85 (-44)	-78 (-38)
USY/ Interaction with one LAS	-154 (-63)	-153 (-29)
HY/ Interaction with one acidic proton	-94 (-52)	-84 (-40)

3.3.4 Effect of the Si/Al ratio on the regeneration capacity

The bulky pyridine molecules ($d_{molecular}$ = 0.56 nm) are assumed to not access the sodalite cage and D6R channels of HY2.5 zeolites. Indeed the quantified OH groups are related to the presence of an aluminum atom in the supercage. Knowing the number of OH groups and the number of supercages per gram of solid, we can evaluate the number of OH groups present per unit cell (8 supercages). From that, we can estimate a percentage of DAY supercages per unit cell for the different zeolites as indicated in Table 6. HY2.5 zeolite has almost 13 OH groups per unit cell where the probability to have a supercage without any proton is very low. For USY zeolites the number of quantified OH groups per unit cell varies between 0.4 and 0.8; which gives a percentage of 90% to 95% of pure siliceous supercages (DAY) in these zeolites. We have already mentioned that the adsorption energies of phenol over a Brønsted acid site for HY and USY zeolites presents similar values (-85 and -94 kJ.mol^{-1}). Moreover, the amount of residual phenol species directly correlates with the amount of quantified acid sites. From that, we can conclude that a high regeneration capacity can be obtained by increasing the amount of pure siliceous cages (DAY cages) in the zeolite. Results in Table 6 show that for a high concentration of DAY cages in the USY zeolites (90 to 95%) the regeneration capacity increases to 73% and 95% in comparison to the HY zeolites (43%).

Table 6 – Percentage of DAY supercages per unit cell of Y and USY zeolites.

Adsorbents	Regeneration capacity (%)	Supercage OH groups per unit cell	DAY supercage (%)

HY2.5	43%	13.3	0%
USY13	73%	0.8	90%
USY22	83%	0.7	91%
USY33	93%	0.6	93%
USY40	95%	0.4	95%

4. Conclusion

The separation of phenol from isooctane by protonic Y zeolites adsorbent with different Si/Al ratios was experimentally and theoretically explored. The phenol adsorption capacity of the different zeolites was demonstrated to be very similar, around 2.2 $mmol.g^{-1}$. Experimental and GCMC approaches showed that this amount corresponds to 3 – 4 phenol molecules adsorbed per supercage. This emphasizes that the Si/Al ratio and the strength of the acid sites do not affect the solid adsorption capacity but rather their diffusion rate. A parallel between experiments and GCMC simulations confirmed that increasing the Si/Al ratio improves the separation of phenol from isooctane as it facilitates the diffusion of phenol inside the porosity.

The solid regeneration under Argon flow at 473K showed that residual phenol molecules remain in interaction with Brønsted and Lewis acid sites. DFT enables us to evaluate the interaction energy of phenol molecules within zeolites. On purely siliceous faujasite, phenol is physically adsorbed (-51 $kJ.mol^{-1}$). In presence of acid sites in the faujasite structure, interaction energies become stronger (around -90 $kJ.mol^{-1}$) which is high enough to create strongly adsorbed phenol species. Over a Lewis acid site, phenol is strongly adsorbed and the interaction energy is equal to -154 $kJ.mol^{-1}$. Note that on USY zeolite with the highest Si/Al ratio the amount of Lewis acid sites is very low. At a high Si/Al ratio, the amount of purely siliceous cages increases, and thus the fraction of physically adsorbed phenol species. Consequently, experiments and theoretical calculations explain why USY zeolite with the highest Si/Al ratio (USY 40) presents the highest regeneration ability. We have shown throughout this work that the use of USY zeolite is very attractive for phenol selective adsorption from isooctane. In a near future we plan to deal with more complex hydrocarbons mixture containing aromatic compounds (40 wt.% of a model biofuel) such as toluene that can competes the phenol adsorption.

5. Acknowledgements

We thank the Labex EMC3 and FEDER for the PhD grant of IK and for their financial support to the BIOCAR project. We also acknowledge the PMMS (Pôle Messin de Modélisation et de Simulation) and GENCI-CCRT (Grant No. x2017-085106 and x2018-085106) for providing us computer time.

6. References

(1) Nabi, M. N.; Rahman, M. M.; Islam, M. A.; Hossain, F. M.; Brooks, P.; Rowlands, W. N.; Tulloch, J.; Ristovski, Z. D.; Brown, R. J. Fuel Characterisation, Engine Performance, Combustion and Exhaust Emissions with a New Renewable Licella Biofuel. *Energy Conversion and Management* **2015**, *96*, 588–598.

(2) Fogassy, G.; Lorentz, C.; Toussaint, G.; Thegarid, N.; Schuurman, Y.; Mirodatos, C. Analytical Techniques Tailored for Biomass Transformation to Biofuels. *Environmental Progress & Sustainable Energy* **2013**, *32* (2), 377–383.

(3) Serrano-Ruiz, J. C.; Dumesic, J. A. Catalytic Routes for the Conversion of Biomass into Liquid Hydrocarbon Transportation Fuels. *Energy Environ. Sci.* **2011**, *4* (1), 83–99.

(4) Bouvier, C.; Romero, Y.; Richard, F.; Brunet, S. Effect of H2S and CO on the Transformation of 2-Ethylphenol as a Model Compound of Bio-Crude over Sulfided Mo-Based Catalysts: Propositions of Promoted Active Sites for Deoxygenation Pathways Based on an Experimental Study. *Green Chemistry* **2011**, *13* (9), 2441.

(5) Quadrelli, E. A. 25 Years of Energy and Green Chemistry: Saving, Storing, Distributing and Using Energy Responsibly. *Green Chemistry* **2016**, *18* (2), 328–330.

(6) Lange, J.-P. Lignocellulose Conversion: An Introduction to Chemistry, Process and Economics. *Biofuels, bioproducts and biorefining* **2007**, *1* (1), 39–48.

(7) Aro, E.-M. From First Generation Biofuels to Advanced Solar Biofuels. *Ambio* **2016**, *45* (S1), 24–31.

(8) Chaudhary, R.; Dhepe, P. L. Solid Base Catalyzed Depolymerization of Lignin into Low Molecular Weight Products. *Green Chemistry* **2017**, *19* (3), 778–788.

(9) Fogassy, G.; Thegarid, N.; Schuurman, Y.; Mirodatos, C. From Biomass to Bio-Gasoline by FCC Co-Processing: Effect of Feed Composition and Catalyst Structure on Product Quality. *Energy & Environmental Science* **2011**, *4* (12), 5068.

(10) Bertero, M.; de la Puente, G.; Sedran, U. Fuels from Bio-Oils: Bio-Oil Production from Different Residual Sources, Characterization and Thermal Conditioning. *Fuel* **2012**, *95*, 263–271.

(11) Huber, G. W.; Iborra, S.; Corma, A. Synthesis of Transportation Fuels from Biomass: Chemistry, Catalysts, and Engineering. *Chemical Reviews* **2006**, *106* (9), 4044–4098.

(12) de Miguel Mercader, F.; Groeneveld, M. J.; Kersten, S. R. A.; Way, N. W. J.; Schaverien, C. J.; Hogendoorn, J. A. Production of Advanced Biofuels: Co-Processing of Upgraded Pyrolysis Oil in Standard Refinery Units. *Applied Catalysis B: Environmental* **2010**, *96* (1–2), 57–66.

(13) Fogassy, G.; Thegarid, N.; Schuurman, Y.; Mirodatos, C. The Fate of Bio-Carbon in FCC Co-Processing Products. *Green Chemistry* **2012**, *14* (5), 1367.

(14) Fornefett, I.; Rabet, D.; Buttersack, C.; Buchholz, K. Adsorption of Sucrose on Zeolites. *Green Chemistry* **2016**, *18* (11), 3378–3388.

(15) Koubaissy, B.; Joly, G.; Batonneau-Gener, I.; Magnoux, P. Adsorptive Removal of Aromatic Compounds Present in Wastewater by Using Dealuminated Faujasite Zeolite. *Industrial & Engineering Chemistry Research* **2011**, *50* (9), 5705–5713.

(16) Khalid, M.; Joly, G.; Renaud, A.; Magnoux, P. Removal of Phenol from Water by Adsorption Using Zeolites. *Industrial & Engineering Chemistry Research* **2004**, *43* (17), 5275–5280.

(17) Van de Voorde, B.; Damasceno Borges, D.; Vermoortele, F.; Wouters, R.; Bozbiyik, B.; Denayer, J.; Taulelle, F.; Martineau, C.; Serre, C.; Maurin, G.; et al. Isolation of Renewable Phenolics by Adsorption on Ultrastable Hydrophobic MIL-140 Metal–Organic Frameworks. *ChemSusChem* **2015**, *8* (18), 3159–3166.
(18) Kujawski, W.; Warszawski, A.; Ratajczak, W.; Porebski, T.; Capa\la, W.; Ostrowska, I. Removal of Phenol from Wastewater by Different Separation Techniques. *Desalination* **2004**, *163* (1–3), 287–296.
(19) Roostaei, N.; Tezel, F. H. Removal of Phenol from Aqueous Solutions by Adsorption. *Journal of Environmental Management* **2004**, *70* (2), 157–164.
(20) Hank, D.; Azi, Z.; Ait Hocine, S.; Chaalal, O.; Hellal, A. Optimization of Phenol Adsorption onto Bentonite by Factorial Design Methodology. *Journal of Industrial and Engineering Chemistry* **2014**, *20* (4), 2256–2263.
(21) Lobban, F. P. Process for Removing Phenols and Mercaptans from Light Petroleum Distillates. 2605212, July 1952.
(22) Schlicht, R. C.; Mccoy, F. C. Selective Adsorption of Phenols from Solution in Hydrocarbons, November 1971.
(23) Cherif, L.; El-Berrichi, F.-Z.; Bengueddach, A.; Tougne, P.; Fraissard, J. Structural Evolution of Calcium-Exchanged (NH4)2SiF6-Dealuminated Y Zeolite after Various Chemical Treatments. *Colloids and Surfaces A: Physicochemical and Engineering Aspects* **2003**, *220* (1–3), 83–89.
(24) López-Fonseca, R.; Gutiérrez-Ortiz, J. I.; Gutiérrez-Ortiz, M. A.; González-Velasco, J. R. Dealuminated Y Zeolites for Destruction of Chlorinated Volatile Organic Compounds. *Journal of Catalysis* **2002**, *209* (1), 145–150.
(25) Bai, P.; Tsapatsis, M.; Siepmann, J. I. TraPPE-Zeo: Transferable Potentials for Phase Equilibria Force Field for All-Silica Zeolites. *The Journal of Physical Chemistry C* **2013**, *117* (46), 24375–24387.
(26) Jousse, F.; Auerbach, S. M.; Vercauteren, D. P. Adsorption Sites and Diffusion Rates of Benzene in HY Zeolite by Force Field Based Simulations. *The Journal of Physical Chemistry B* **2000**, *104* (10), 2360–2370.
(27) Rai, N.; Siepmann, J. I. Transferable Potentials for Phase Equilibria. 10. Explicit-Hydrogen Description of Substituted Benzenes and Polycyclic Aromatic Compounds. *The Journal of Physical Chemistry B* **2013**, *117* (1), 273–288.
(28) Potoff, J. J.; Siepmann, J. I. Vapor–Liquid Equilibria of Mixtures Containing Alkanes, Carbon Dioxide, and Nitrogen. *AIChE Journal* **2001**, *47* (7), 1676–1682.
(29) Lorentz, H. A. Ueber die Anwendung des Satzes vom Virial in der kinetischen Theorie der Gase. *Annalen der Physik* **1881**, *248* (1), 127–136.
(30) Berthelot, D. Sur les mélanges des gaz. *Comptes Rendus hebdomadaires des séances de l'1cadémie des Sciences* **1898**, *126*, 1703.
(31) Vlugt, T. J. H.; García-Pérez, E.; Dubbeldam, D.; Ban, S.; Calero, S. Computing the Heat of Adsorption Using Molecular Simulations: The Effect of Strong Coulombic Interactions. *Journal of Chemical Theory and Computation* **2008**, *4* (7), 1107–1118.
(32) Kresse, G.; Hafner, J. Ab Initio Molecular Dynamics for Liquid Metals. *Phys. Rev. B* **1993**, *47* (1), 558–561.
(33) Kresse, G.; Hafner, J. *Ab Initio* Molecular-Dynamics Simulation of the Liquid-Metal–Amorphous-Semiconductor Transition in Germanium. *Physical Review B* **1994**, *49* (20), 14251–14269.
(34) Kresse, G.; Furthmüller, J. Efficient Iterative Schemes for *Ab Initio* Total-Energy Calculations Using a Plane-Wave Basis Set. *Physical Review B* **1996**, *54* (16), 11169–11186.
(35) Bucko, T.; Benco, L.; Hafner, J.; Angyan, J. Proton Exchange of Small Hydrocarbons over Acidic Chabazite: Ab Initio Study of Entropic Effects. *Journal of Catalysis* **2007**, *250* (1), 171–183.
(36) Perdew, J. P.; Burke, K.; Ernzerhof, M. Generalized Gradient Approximation Made Simple. *Phys. Rev. Lett.* **1996**, *77* (18), 3865–3868.
(37) Blöchl, P. E. Projector Augmented-Wave Method. *Phys. Rev. B* **1994**, *50* (24), 17953–17979.

(38) Kresse, G.; Joubert, D. From Ultrasoft Pseudopotentials to the Projector Augmented-Wave Method. *Phys. Rev. B* **1999**, *59* (3), 1758–1775.
(39) Grimme, S. Semiempirical GGA-Type Density Functional Constructed with a Long-Range Dispersion Correction. *J. Comput. Chem.* **2006**, *27* (15), 1787–1799.
(40) Gould, T.; Lebègue, S.; Ángyán, J. G.; Bučko, T. A Fractionally Ionic Approach to Polarizability and van Der Waals Many-Body Dispersion Calculations. *J. Chem. Theory Comput.* **2016**, *12* (12), 5920–5930.
(41) Tkatchenko, A.; DiStasio, R. A.; Car, R.; Scheffler, M. Accurate and Efficient Method for Many-Body van Der Waals Interactions. *Physical Review Letters* **2012**, *108* (23).
(42) Bučko, T.; Hafner, J.; Lebègue, S.; Ángyán, J. G. Improved Description of the Structure of Molecular and Layered Crystals: Ab Initio DFT Calculations with van Der Waals Corrections. *J. Phys. Chem. A* **2010**, *114* (43), 11814–11824.
(43) Bučko, T.; Lebègue, S.; Gould, T.; Ángyán, J. G. Many-Body Dispersion Corrections for Periodic Systems: An Efficient Reciprocal Space Implementation. *J. Phys.: Condens. Matter* **2016**, *28* (4), 045201.
(44) Chebbi, M.; Chibani, S.; Paul, J.-F.; Cantrel, L.; Badawi, M. Evaluation of Volatile Iodine Trapping in Presence of Contaminants: A Periodic DFT Study on Cation Exchanged-Faujasite. *Microporous and Mesoporous Materials* **2017**, *239*, 111–122.
(45) Van Speybroeck, V.; Hemelsoet, K.; Joos, L.; Waroquier, M.; Bell, R. G.; Catlow, C. R. A. Advances in Theory and Their Application within the Field of Zeolite Chemistry. *Chemical Society Reviews* **2015**, *44* (20), 7044–7111.
(46) Chibani, S.; Medlej, I.; Lebègue, S.; Ángyán, J. G.; Cantrel, L.; Badawi, M. Performance of Cu^{II} -, Pb^{II} -, and Hg^{II} -Exchanged Mordenite in the Adsorption of I_2, ICH_3, H_2O, CO, $ClCH_3$, and Cl_2: A Density Functional Study. *ChemPhysChem* **2017**, *18* (12), 1642–1652.
(47) Maurin, G.; Llewellyn, P. L.; Bell, R. G. Adsorption Mechanism of Carbon Dioxide in Faujasites: Grand Canonical Monte Carlo Simulations and Microcalorimetry Measurements. *J. Phys. Chem. B* **2005**, *109* (33), 16084–16091.
(48) Maurin, G.; Bell, R.; Kuchta, B.; Poyet, T.; Llewellyn, P. Adsorption of Non Polar and Quadrupolar Gases in Siliceous Faujasite: Molecular Simulations and Experiments. *Adsorption* **2005**, *11* (S1), 331–336.
(49) Sastre, G.; Katada, N.; Suzuki, K.; Niwa, M. Computational Study of Brønsted Acidity of Faujasite. Effect of the Al Content on the Infrared OH Stretching Frequencies. *The Journal of Physical Chemistry C* **2008**, *112* (49), 19293–19301.
(50) Janssen, A. H.; Koster, A. J.; de Jong, K. P. Three-Dimensional Transmission Electron Microscopic Observations of Mesopores in Dealuminated Zeolite Y. *Angewandte Chemie* **2001**, *113* (6), 1136–1138.
(51) Malicki, N.; Mali, G.; Quoineaud, A.-A.; Bourges, P.; Simon, L. J.; Thibault-Starzyk, F.; Fernandez, C. Aluminium Triplets in Dealuminated Zeolites Detected by 27Al NMR Correlation Spectroscopy. *Microporous and Mesoporous Materials* **2010**, *129* (1–2), 100–105.
(52) Khabtou, S.; Chevreau, T.; Lavalley, J. C. Quantitative Infrared Study of the Distinct Acidic Hydroxyl Groups Contained in Modified Y Zeolites. *Microporous Materials* **1994**, *3* (1–2), 133–148.
(53) Leyva, C.; Ancheyta, J.; Travert, A.; Maugé, F.; Mariey, L.; Ramírez, J.; Rana, M. S. Activity and Surface Properties of NiMo/SiO2–Al2O3 Catalysts for Hydroprocessing of Heavy Oils. *Applied Catalysis A: General* **2012**, *425–426*, 1–12.
(54) Maache, M.; Janin, A.; Lavalley, J. C.; Benazzi, E. FT Infrared Study of Brønsted Acidity of H-Mordenites: Heterogeneity and Effect of Dealumination. *butterworth-heinemann* **1995**, 507–516.
(55) Thibault-Starzyk, F.; Gil, B.; Aiello, S.; Chevreau, T.; Gilson, J.-P. In Situ Thermogravimetry in an Infrared Spectrometer: An Answer to Quantitative Spectroscopy of Adsorbed Species on Heterogeneous Catalysts. *Microporous and Mesoporous Materials* **2004**, *67* (1), 107–112.
(56) Moradi, F.; Ganji, M. D.; Sarrafi, Y. Tunable Phenol Remediation from Wastewater Using SWCNT-Based, Sub-Nanometer Porous Membranes: Reactive Molecular Dynamics Simulations and DFT Calculations. *Physical Chemistry Chemical Physics* **2017**, *19* (12), 8388–8399.

(57) Baerlocher, C.; McCusker, L. B.; Olson, D. H. *Atlas of Zeolite Framework Types*, 6th rev. ed.; Elsevier, page 141: Amsterdam, 2007.
(58) Estephane, J.; Groppo, E.; Damin, A.; Vitillo, J. G.; Gianolio, D.; Lamberti, C.; Bordiga, S.; Prestipino, C.; Nikitenko, S.; Quadrelli, E. A.; et al. Structure and Enhanced Reactivity of Chromocene Carbonyl Confined inside Cavities of NaY Zeolite. *The Journal of Physical Chemistry C* **2009**, *113* (17), 7305–7315.
(59) Magnoux, P.; Cartraud, P.; Mignard, S.; Guisnet, M. Coking, Aging, and Regeneration of Zeolites. *journal of catalysis* **1987**, *106*, 242–250.
(60) Jentys, A.; Pham, N. H.; Vinek, H. Nature of Hydroxy Groups in MCM-41. *Journal of the Chemical Society, Faraday Transactions* **1996**, *92* (17), 3287.

Nomenclature

FT-IR	Fourier Transform - Infrared Spectroscopy
DFT	Density Functional Theory
IR	Infrared Spectroscopy
GCMC	Grand Canonical Monte Carlo
USY	Ultra-Stable Y Zeolite
EFAL	Extra Framework Aluminum
VASP	Vienna *Ab initio* Simulation Package
MCT	Mercury Cadmium Telluride detector
VGO	Vacuum Gas Oil
FCC	Fluid Catalytic Cracking
HDO	Hydrodeoxygenation
VLE	vapor-liquid equilibrium